PUBLICATIONS OF THE ASTRONOMICAL SOCIETY OF THE PACIFIC, **114**:153–168, 2002 February
© 2002. The Astronomical Society of the Pacific. All rights reserved. Printed in U.S.A.

TEXES: A Sensitive High-Resolution Grating Spectrograph for the Mid-Infrared

J. H. LACY, M. J. RICHTER, T. K. GREATHOUSE, D. T. JAFFE, AND Q. ZHU
Department of Astronomy, University of Texas at Austin, RLM 15.308, C-1400, Austin, TX 78712-1083; lacy@astro.as.utexas.edu, richter@astro.as.utexas.edu, tommyg@astro.as.utexas.edu, dtj@astro.as.utexas.edu, zhuqf@astro.as.utexas.edu

Received 2001 August 27; accepted 2001 November 14

ABSTRACT. We discuss the design and performance of TEXES, the Texas Echelon Cross Echelle Spectrograph. TEXES is a mid-infrared (5–25 μm) spectrograph with several operating modes: high resolution, cross-dispersed with a resolving power of $R = \lambda/\delta\lambda \approx 100{,}000$, 0.5% spectral coverage, and a ~$1''.5 \times 8''$ slit; medium resolution, long-slit with $R \approx 15{,}000$, 0.5% coverage, and a ~$1''.5 \times 45''$ slit; low-resolution, long-slit with $\delta\lambda \approx 0.004$ μm, 0.25 μm coverage, and a ~$1''.5 \times 45''$ slit; and source acquisition imaging with $0''.33$ pixels and a $25'' \times 25''$ field of view on a 3 m telescope. TEXES has been used at the McDonald Observatory 2.7 m and the NASA Infrared Telescope Facility 3 m telescopes and has proved to be both sensitive and versatile.

1. INTRODUCTION

The mid-infrared spectral region (5–25 μm) is relatively underutilized for astronomical observations, especially at high spectral resolution. The reason for this is largely technical: Earth's 300 K blackbody peaks in this region, resulting in high background and high photon shot noise. In addition, heterodyne spectrometers commonly used at longer wavelengths are relatively insensitive in the mid-infrared, whereas dispersive spectrographs used at visible wavelengths become quite large when used at very high resolution in the mid-infrared.

Although difficult, mid-infrared spectroscopy provides significant, and sometimes unique, astronomical information. The majority of spectral features in the mid-infrared fall into three classes: emission and absorption by grains and very large molecules; fine-structure and recombination line emission by ions; and emission and absorption by molecules, mostly through their vibration-rotation bands. The spectrometers on the *Infrared Space Observatory* (*ISO*) satellite were well suited for the study of solid-state features of dust grains and icy grain mantles and the similar features of very large molecules such as polycyclic aromatic hydrocarbons. These features are relatively broad ($\Delta\lambda/\lambda \approx 1\%$–$10\%$) and so were well resolved by the *ISO* short-wavelength spectrometer with $R = \lambda/\delta\lambda \approx 2000$. The *Space Infrared Telescope Facility* (*SIRTF*), with $R \approx 600$ and much better sensitivity than can be achieved from the ground, will continue this study. However, neither of these spacecraft spectrometers was optimized for studies of narrow gas-phase lines.

Mid-infrared ionic lines have been studied in a number of sources by several ground-based instruments, as well as by *ISO*. These lines provide information similar to that obtained from visible-wavelength forbidden and recombination lines but can be studied in much more obscured sources. With widths ≈10–100 km s^{-1} (the latter in external galaxies), these lines are best studied by instruments with $R \sim 10^4$. Our previous instrument, Irshell (Lacy et al. 1989), was optimized for the study of these lines. *ISO* greatly expanded on the earlier ground-based work, as will *SIRTF*, although the lower resolution on the space-based mid-IR spectrometers is insufficient for detailed kinematic studies.

Less work has been done on molecular lines in the mid-infrared. In molecular clouds these lines have widths of only a few kilometers per second, requiring $R \geq 100{,}000$ for optimal sensitivity and to obtain kinematic information in line profiles. Although a few instruments have achieved such high resolution in the mid-infrared (heterodyne spectrometers, e.g., Mumma et al. 1982, and Fourier transform spectrometers, e.g., Ridgway & Brault 1984), the sensitivity of these instruments was sufficient for the study of only a few of the brightest objects in the sky. Considerable work has been done with *ISO* (e.g., Lahuis & van Dishoeck 2000) concentrating on the many lines of molecular *Q*-branches. Using Irshell, with $R \approx 10{,}000$, we observed interstellar C_2H_2 and CH_4, as well as several other molecules, but could not resolve the individual lines except in regions of shocks or rapid outflows. As a result, we were limited to measurements of equivalent widths of often saturated lines. From this experience we concluded that whereas space-based spectrometers will improve on our observations of solid-state and ionic lines, at least in cases in which high spatial resolution is not required, a high spectral resolution and high-sensitivity ground-based (or airborne) spectrograph was required to further the study of molecules in the infrared.

2. INSTRUMENT DESIGN CHOICES

The biggest difference between the mid-infrared and visible spectral regions, from the point of view of instrument design, is the large amount of thermal background radiation in the mid-infrared. Consequently, mid-infrared instruments must be cooled whenever possible. Even with a fully cryogenic spectrograph, photon shot noise in the background from the telescope and atmosphere is the dominant source of noise in an instrument using a state-of-the-art detector. (Heterodyne spectrometers, with additional quantum noise, are the exception to this statement.)

Several types of spectrometers are capable of $R = 100{,}000$, with each having advantages and disadvantages. Heterodyne spectrometers can easily achieve even higher resolution but have the disadvantage of observing only a diffraction-limited field in the sky and having quantum noise much greater than background photon noise in the mid-infrared. Fabry-Pérot spectrometers are scanning monochromators (although with slightly different wavelengths transmitted at different field positions) and so must observe different wavelengths sequentially. This inefficiency can be overcome by the efficiency of observing many field positions simultaneously with a detector array if information about different field positions is of interest. An additional drawback to the use of Fabry-Pérot spectrometers for very high resolution infrared work is that several interferometers must be used in series to isolate a single transmission spike of the high-order interferometer, and each of the interferometers must be cooled to avoid excess photon noise. Fourier transform spectrometers can also achieve the desired resolution with sufficiently long path length modulation (1 m for $R = 100{,}000$ at $\lambda = 10\ \mu$m). They have the disadvantage of receiving background radiation from the entire spectral region observed, resulting in increased photon noise, which cancels their multiplex advantage and gives them a sensitivity equal to that of a scanning monochromator. Finally, grating spectrographs also can be used for very high resolution spectroscopy. When used with detector arrays, grating spectrographs have the advantage of observing many spectral elements simultaneously, while observing a line of field positions along a narrow slit.

These sensitivity arguments led us to limit our choice of spectrometer to Fabry-Pérots and gratings. The choice between these two options was based on the relative importance of simultaneous observations of a two-dimensional field versus simultaneous spectral and one-dimensional spatial observations. We decided in favor of the latter, and thus in favor of a grating spectrograph, based on the fact that molecular lines, for which very high resolution is most often needed, are often seen in absorption against nearly pointlike continuum sources.

The primary difficulty in using a grating spectrograph for very high resolution spectroscopy in the mid-infrared is that a very large grating is needed. The maximum theoretical, or diffraction-limited, resolving power of a grating is determined by the product of the number of grooves illuminated and the diffraction order, or equivalently the optical path difference in waves between the two ends of the grating,

$$R_{\text{diff-ltd}} = 2nl/d = 2l\sin\theta/\lambda, \qquad (1)$$

where n is the diffraction order number, l is the illuminated length, d is the groove spacing, and θ is the incidence angle from normal. In practice, diffraction-limited resolution is never achieved without intolerable light loss at the entrance slit, making $R \approx l/\lambda$ a reasonable approximation. This means that achieving $R = 100{,}000$ at $\lambda = 10\ \mu$m requires a grating approximately 1 m in length.

Beyond the fabrication of the grating, the primary problem in making a very high resolution mid-infrared spectrograph is in designing an optical layout that uses it efficiently and that can be cryogenically cooled in a reasonably sized Dewar. Most high-resolution grating spectrographs use echelle gratings with blaze angles between $\theta = 63\overset{\circ}{.}4$ ($\tan\theta = 2$ or R2) and $\theta = 76\overset{\circ}{.}0$ (R4). Unless used with anamorphic optics, these gratings and the light beams that illuminate them must have widths $\frac{1}{2}$–$\frac{1}{4}$ of the grating length for optimum illumination. A very large Dewar would be required to contain the resulting spectrograph. This problem can be ameliorated by using a more steeply blazed grating. We chose to use an R10 grating ($\theta = 84\overset{\circ}{.}3$), requiring a light-beam diameter only 1/10 the grating length. Our grating is 36 inches long and 3.4 inches wide. It is illuminated by a 3.3 inch diameter beam formed by a 40 inch focal length mirror collimating f/12 light (slightly underilluminating the grating to improve its efficiency at the expense of a small decrease in resolution). The entire instrument fits inside a 1.5 m long, 0.4 m diameter liquid-helium (LHe) Dewar.

There are several drawbacks to using such a steeply blazed grating. First, unless the grating is used in very high order, the angular width of an order can be comparable to the angle between grazing incidence and the blaze (~6° in our case), resulting in a large variation in resolution across an order. And second, the tilt of the slit image resulting from the shift in wavelength with out-of-plane angle is proportional to the product of the out-of-plane angle and $\tan\theta$ (the R number) and can be very large unless the grating is used very close to Littrow. (If, instead, input and output beams are separated in the plane of dispersion, groove shadowing can be significant.) We avoided the first problem by having a coarse grating with 0.3 inch (7.62 mm) groove spacing, implying a diffraction order of $n \approx 1500$ at $\lambda = 10\ \mu$m. The angular width of an order, the single-slit diffraction pattern from a groove face, is then $\Delta\phi = (\tan\theta)\lambda/d = 0\overset{\circ}{.}75$. This is small enough that the resolution variation across the order is tolerable. We minimized the second problem by using an out-of-plane angle of 0.01 rad, although the slit image rotation is still $2(\tan\theta)\gamma = 12°$.

A very coarse ruling has the additional advantage of very small order spacing. The spectral width of a grating order is given by $\Delta\nu = \nu/n$, or $\Delta w\ (\text{cm}^{-1}) = 1/2d$. The number of diffraction-limited resolution elements in an order is equal to the number of illuminated grooves in the grating, or $n_{\text{res. el.}} = l/d = 120$. The small-order spacing and number of resolution elements per order are optimally matched to the 256 pixels across the available detector array, allowing Nyquist sampling of the diffraction spot and complete coverage of an order with appropriate optics (although not at all wavelengths since the width of a diffraction spot and an order scale in proportion to wavelength). Consequently, it is possible to cross-disperse the spectrum and obtain continuous spectral coverage, without gaps between orders. Furthermore, the grating is held at a fixed angle, thus simplifying the mounting mechanism.

In the remainder of this paper we describe TEXES, the Texas Echelon Cross Echelle Spectrograph. TEXES uses the long, coarsely ruled grating described here, which we refer to as an echelon, as its primary disperser and an echelle grating used in low order as a cross-disperser to achieve our goal of $R = 100{,}000$ in the mid-infrared. TEXES also has other modes of operation for lower resolution observations.

3. DESIGN

3.1. Optical Design

TEXES is an up-looking instrument used at Cassegrain focus. It is in an LHe-cooled Dewar with cold foreoptics and two spectrograph chambers. The first chamber houses the high-resolution echelon grating. The second chamber contains cross-dispersion gratings and the detector.

Figures 1 and 2 show the light path through the spectrograph. Light enters the Dewar through a focusable, up-looking warm lens. This lens forms an image of the telescope entrance pupil on a cold Lyot stop. It has little effect on the location of the focal plane, which lies just inside the Dewar. A second (cold) lens reimages the focal plane at f/12 off the first fold mirror, through a filter wheel, and onto the slit wheel. ZnSe lenses are installed if the longest wavelength of interest is less than 14 μm, and KBr is used for longer wavelength observations.

After passing through the slit, the light enters the echelon chamber, where it is reflected by a flat fold mirror and a 40 inch focal length, off-axis paraboloidal collimator to the echelon grating. The echelon is used at a steep angle, $84\overset{\circ}{.}3$, as discussed in § 2. The dispersed light returns to the collimator, then to a second folding flat, which reflects it out of the echelon chamber through a port opposite the slit. It then enters the cross-dispersion chamber, with a similar paraboloid-grating-paraboloid arrangement, but turned by 90°. The light is reflected through a focal reduction lens to the detector (see Fig. 2), a 256×256, 30 μm pixel SiAs array (see § 4.1). The focal reducer changes the f/12 beam to f/6 so that the detector Nyquist samples the diffraction pattern at $\lambda \geq 10$ μm.

A 31.6 groove mm^{-1} R4 echelle, with a length-to-width ratio of 2, is most often used for cross-dispersion. The R4 grating was actually a result of a purchasing error; an R2 grating was specified, but fortuitously R4 gratings in which both sides of the grooves are efficient, as is the case with this grating in the infrared, have good efficiency in Littrow configuration over a wide range of incidence angles near R2 because of corner reflection by the grooves. The cross-dispersion grating separates the echelon orders by ∼20 diffraction-limited resolution elements, allowing a sufficient slit length for nodding compact objects along the slit or mapping of slightly extended objects. The spectral coverage is typically $\lambda/200$, which includes 5–10 echelon orders, depending on wavelength. A full echelon order lands on the detector for $\lambda < 11$ μm, giving continuous coverage at short wavelengths, but gaps occur between orders at longer wavelengths.

Several positionable optics allow the instrument to be used in other modes, for long-slit, lower resolution spectroscopy and for imaging. First, the two folding flats in the echelon chamber are mounted on a rotatable assembly. When this assembly is rotated by 45°, the incoming, diverging light is sent to a concave spherical mirror, which reflects it back to a convex sphere mounted on the rotating assembly between the two folding flats. It then returns to the concave sphere and from there to the second flat. This arrangement forms an Offner relay, which reimages the slit onto the output aperture of the echelon chamber, while acting like a K mirror that rotates the slit image by 90° so that it is perpendicular to the dispersion of the echelle grating. In this arrangement the instrument is a medium-resolution spectrograph with $R \approx 15{,}000$ and a spectral coverage the same as in cross-dispersed mode. Because only one order of the echelle is used, the entire 8 mm ($45''$ on a 3 m telescope) slit length can be used. A second long-slit mode can be chosen by swinging a first-order grating into the light beam in front of the echelle. This 75 groove mm^{-1} R0.5 grating gives a resolution of 0.004 μm and a spectral coverage of 0.25 μm in first order (at 8–14 μm). The low-resolution grating can also be used as a cross-disperser for the echelon, providing 0.25 μm (or ∼40 echelon orders) of coverage but requiring a very short slit or pinhole aperture to separate the orders. In addition to the various spectrographic instrument modes, the instrument can be used as a low-efficiency camera by bypassing the echelon and turning the low-resolution grating face-on so that it acts as a mirror. This mode, which is used for source acquisition, has good image quality and $0\overset{''}{.}33$ pixels on a 3 m telescope but only a $\sim 25'' \times 25''$ field of view and low efficiency compared to an optimized camera. In a variation on the imaging mode, the K-mirror assembly can be rotated an additional 45° for a pupil imaging mode (see Fig. 2). A pair of flat mirrors and a lens then image the instrument cold stop, rather than the focal plane or slit, at the output of the echelon chamber. With the low-resolution grating face-on, this image of the Lyot stop and telescope pupil (the secondary mirror) is reimaged on the detector. This mode simplifies alignment of the instrument with the telescope.

Ray-trace calculations show that the optical design is diffraction-limited in all modes down to a 5 μm wavelength over a 1×1 cm ($100'' \times 100''$ on a 3 m telescope) focal plane. The calculated spectral resolution of the echelon when used with a diffraction-limited slit is 0.007 cm^{-1}, or $R = 140{,}000$ at $\lambda = 10$ μm. Laboratory tests with visible, near-IR, and mid-IR lasers indicate slight phase errors over portions of the echelon. Modeling suggests that these errors increase the relative strength of sidelobes at shorter wavelengths, but the majority of the power should remain in the central diffraction peak down to a ∼5 μm wavelength. Since the detector pixels Nyquist-sample the diffraction pattern only at 10 μm and longward, the

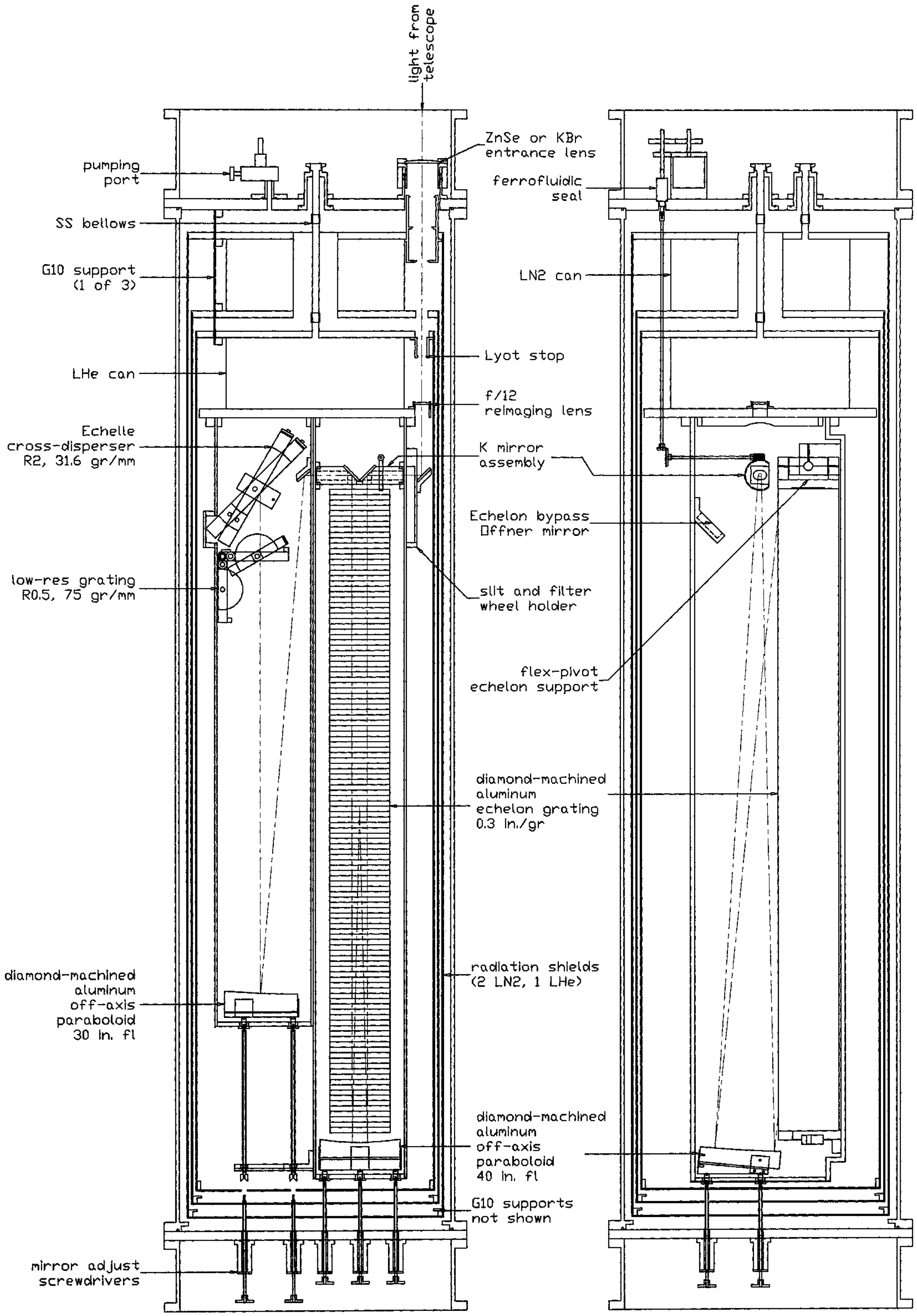

FIG. 1.—Two views of the TEXES Dewar and optics, with many structural details omitted for clarity. The dot-dashed line shows the path of the light through the system in the high-resolution cross-dispersed mode. The low-resolution grating is folded down and out of the light path in this mode.

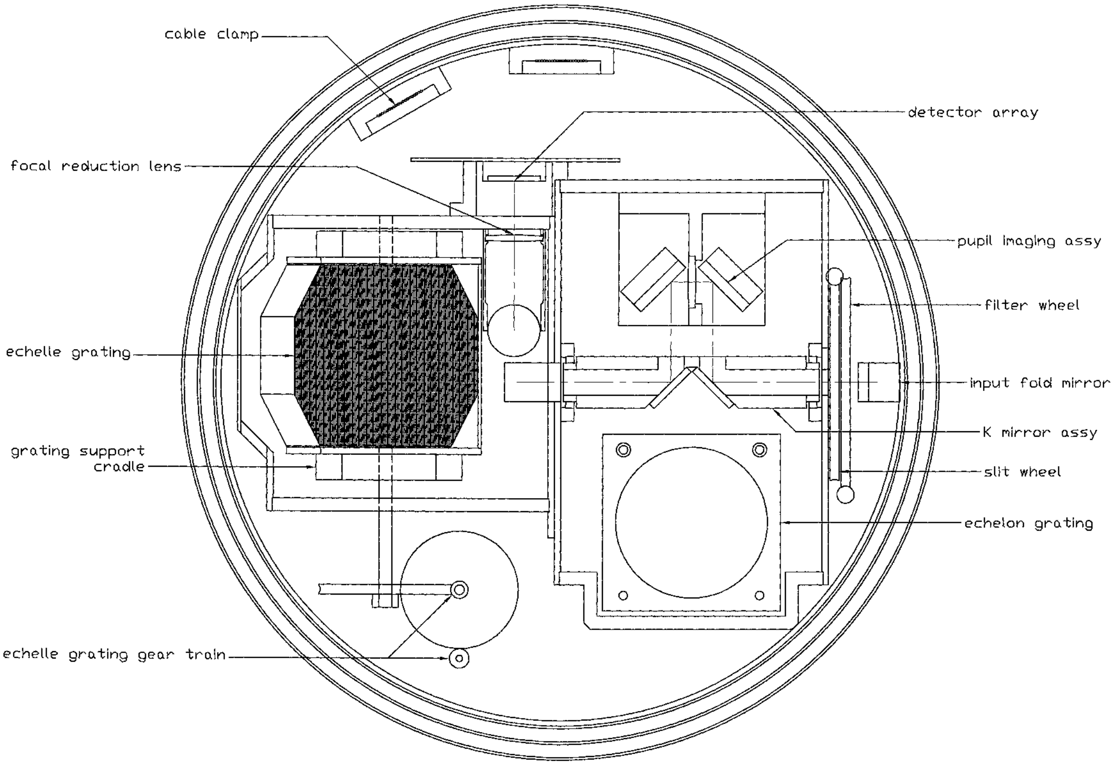

FIG. 2.—View of the TEXES optics looking toward the LHe work surface. The two off-axis paraboloids have been omitted from this view. The K-mirror assembly is shown rotated to the position that causes the light to pass through the pupil imaging mirrors and lens.

resolution is effectively limited to the 10 μm diffraction limit. For a description of the actual system performance, see § 6.

3.2. Echelon Grating

The idea of making a very coarsely ruled diffraction grating was suggested by Michelson (1898). He attempted to make such a grating by stacking a number of glass plates of equal thickness to make what was essentially a grism. He referred to the device as an echelon, because of the staggered arrangement of the plates. Subsequently, reflection echelons were made (see Born & Wolf 1980) but were limited to a moderate number of reflecting faces.

In 1993 we undertook to assemble a reflecting echelon grating using 100 diamond-machined aluminum facets for the mirror surfaces, spaced by 0.4 inches along a 40 inch aluminum support bar. Although an echelon of this size had not previously been made, we felt that the reduced precision required for infrared use would make it feasible. In fact, we demonstrated that we were able to attach facets to the bar with the required precision. Unfortunately, the additional requirement that the echelon had to remain aligned during repeated cycling between 300 and 4 K for use in the thermal infrared more than compensated for the advantage of relaxed tolerance. The motion of the facets during cooldown (~1 μm rms) was several times what we could tolerate. The process of assembling and testing the echelon is described in more detail by Lacy et al. (1998).

Fortunately, during the time we were attempting to assemble an echelon grating, B. W. and K. G. Bach at Hyperfine, Inc., were developing the capability of diamond machining gratings of this size. In 1998 we placed an order for a 36 inch long, 3.4 inch wide, R10 grating with 0.3 inch groove spacing. An excellent grating for our purposes was received in 1999. The diamond machining and the capabilities of Hyperfine are described by Bach, Bach, & Bach (2000). (Properly speaking, the diamond-machined grating is not really an echelon because it is not assembled from separate mirrors, but we continue to refer to it by that name, not wanting to have to change the name of our instrument.)

Some care was taken in preparing the substrate before diamond machining to avoid distortion during machining or cooling. Our main worry was that stress variations introduced into the substrate during heat treating would be relieved during machining, thermal cycling, or aging. We took several steps to avoid this. First, the substrate was cut from a large 6061 T6 aluminum tooling plate, oriented so that the surface to be diamond machined was inside the plate (not on the top or bottom) so the diamond machining would not remove material with atypical heat-treating stresses. A 2.9 inch diameter hole was then gun-drilled through the length of the 3.4 × 3.4 × 36 inch substrate, removing about one-half of its mass but little of its stiffness. It was then given a stress-relief anneal (650°F for ∼2 hr, followed by slow cooling; Gassner et al. 1964). After that, the substrate was cycled 5 times between 210°F and a liquid nitrogen bath, with the heating and cooling each taking several hours. Finally, the grating surface was diamond machined. In the 2 yr since then it has been cycled between 300 and 4 K ∼15 times, with no detectable changes.

The echelon's intrinsic stiffness and the fact that it is fixed in place, a consequence of the small angular size of the orders, simplify mounting. We support the echelon purely at its ends, and it does not sag detectably under gravity, even when in a horizontal orientation (equivalent to pointing at the horizon when on the telescope). The mounts to the support structure are designed not to overconstrain the echelon (see Fig. 1). At the top end, we use flex pivots (not shown) to constrain 4 degrees of freedom. At the bottom end, we use a piece of aluminum that is necked down so that only the remaining 2 degrees of freedom are constrained. In this piece, some effort was made to maximize its thermal cross section since this is the main path for heat to flow out of the echelon. (In retrospect, the supports should have been swapped for faster cooldown.)

3.3. Mechanical Design

Working in the thermal infrared near 10 μm requires the cooling of instrument optics to well below liquid-nitrogen (LN_2) temperature to reduce background radiation. TEXES has an LHe-cooled inner chamber surrounded by walls that are heat sunk to an LN_2 Dewar, all contained in a large vacuum jacket (see Fig. 1). The LHe Dewar bottom surface serves as the cold surface for mounting the optical chambers. The LN_2 Dewar has two cold shields connected to it. The outer shield must conduct the radiative heat load from the warm vacuum wall along the length of the Dewar up to the nitrogen vessel. This outer shield will thus not be at LN_2 temperature at its far end. In a Dewar of the length of TEXES (1.5 m), the heat flux onto the LHe-cooled chamber from a single LN_2-cooled shield would significantly increase LHe boiloff. To prevent this we use a second, inner, LN_2 shield attached to the bottom of the LN_2 reservoir. Since this shield is protected from room-temperature radiation by the outer LN_2 shield, it is essentially isothermal with the LN_2 reservoir. To further reduce the heat load on the LHe, we pump on the LN_2 Dewar to drop its temperature by ∼10 K. The hold time of the 5 liter LN_2 Dewar is 16–24 hr, while the 5 liter LHe Dewar's hold time is about 2 days. It takes 4–5 days, ∼100 liters LN_2, and ∼30 liters LHe to evacuate and cool the Dewar to operational temperatures. To minimize LHe usage, we thoroughly cold soak the Dewar with pumped LN_2 in the LHe reservoir, although care must be taken to make sure no residual LN_2 is in the reservoir when starting the LHe transfer. The Dewar was produced by Precision Cryogenic Systems, Inc.

G10 fiberglass supports are used to separate the LN_2 Dewar from the outer vacuum wall and the LHe Dewar from the LN_2 Dewar. The TEXES G10 support is made of three long tabs that connect to the vacuum jacket, the nitrogen can twice, and then to the helium can (Fig. 1). This design is less prone to failure than the 6-tab used in our previous instrument (Lacy et al. 1989). However, tension in the tabs can cause them to slip at their clamps, resulting in screw tear-out when assembling the Dewar on its side, or misalignment when on the telescope. The screw tear-out problem was fixed by doubling the G10 thickness at the screws, but slippage causing misalignment has still been an occasional problem.

All internal mechanisms have external motors driving fiberglass shafts coupled to stainless steel shafts. Ferrofluidic vacuum feedthroughs couple the motors with the fiberglass shafts. There are five internal mechanisms: filter wheel, slit wheel, rotating K-mirror assembly, and two cross-dispersion gratings. The motors are geared down inside the LHe temperature region after the connection to the stainless steel shafts, thus reducing the effect of windup in the fiberglass shafts. Both spur and worm gears are used. Brass wipers connected to the nitrogen Dewar and pressing up against the fiberglass shafts reduce the heat flow into the LHe.

The K-mirror assembly and both cross-dispersion gratings are supported by degreased ball bearing assemblies. The slit and filter wheels are each supported by stainless steel balls set into cups machined into the ends of the wheel's axles. The axles are press-fitted into the wheels. This design is quite simple and takes little space.

The parabolic mirror at the end of each chamber is mounted to a backup plate attached to the chamber end plate with a sandwich of stainless steel and copper leaf springs. The mirrors rest on three screws that can be adjusted by retractable screwdrivers that enter the vacuum chamber through O-ring seals. On the three-point mounts, the mirrors can be moderately translated in the focus direction and tipped for optical alignment. The echelon chamber paraboloid can be tipped to observe wavelengths that would normally fall off our detector, which can occur at wavelengths longer than 11 μm.

The slit wheel is made of a 3.5 inch diameter brass worm wheel, a slit mask, and a brass insert that mates the two together. There are 18 slit positions on the mask spaced at 20° intervals: open, three pinholes, seven long slits, and seven short slits. The slits were made using photolithography on a 0.1 mm thick piece of brass by Photo Design of Arizona, Inc. The slit mask is soldered to the backing insert, which is screwed into the worm wheel. Slit widths range from 120 μm (2 pixels) to 550 μm (9 pixels).

The filter/decker wheel comes just before the slit wheel. Filters are needed to isolate echelle orders. There are seven discrete filters and two circular variable filters (CVFs), all purchased from the (no longer available) stock filter selection of Optical Coating Labs, Inc. Each discrete filter is covered with a decker mask, which defines four different slit lengths for high-resolution mode and a long-slit position for medium- and low-resolution modes. Different slit lengths are needed in high-resolution mode because of the varying angular separation between echelon orders as the wavelength or echelle angle is changed. Typical lengths range from 6″ at short wavelengths to 12″ at long wavelengths. Each CVF has a single slit length appropriate for the short-wavelength end of its range ($4\farcs5$ and 6″). The available filters and slit lengths are listed in Table 1.

TABLE 1
FILTERS AND SLIT LENGTHS

Wavelength Range (μm)	Slit Lengths[a] (arcsec)
7.5–8.5	4.4, 6.0, 7.7, 9.3, 45
8.4–9.2	4.4, 6.0, 7.7, 9.3, 45
9.4–11.4	5.0, 6.6, 8.5, 10.4, 45
11.2–12.2	5.5, 7.1, 12.1, 16.5, 45
11.7–14.2	6.0, 8.0, 9.9, 11.8, 45
17–22	11.5, 14.6, 18.1, 22.0, 45
8–13	45
4–8 CVF[b]	4.4
8–14 CVF[b]	5.5

[a] Medium- and low-resolution modes use the 45″ slits. In high-resolution mode, the slit length used depends on the angle, and thus the resolving power, of the cross-disperser.

[b] CVFs are ~1.5% bandwidth.

4. DATA ACQUISITION SYSTEM

4.1. Detector

The detector, electronics, and software for TEXES are to be shared with EXES, a very similar spectrograph being developed for use on SOFIA, the Stratospheric Observatory for Infrared Astronomy (Becklin 1997). The combined science goals for EXES and TEXES drive both our choice of detector and the requirements for the readout electronics. For the detector, the requirement that EXES have good sensitivity at high spectral resolution in the 5.5 μm $\leq \lambda \leq$ 7 μm range was a critical factor. The combination of high spectral resolution, short wavelengths, and detector response as a function of wavelength results in a low rate of background electrons: 350 e^- s^{-1} pixel^{-1}. To ensure that our instrument is background noise limited, we must have a detector with very low dark current and read noise.

We chose the Raytheon 256^2 SiAs IBC "*SIRTF*" array with the CRC-744 readout integrated circuit (Wu et al. 1997). We received our science grade array in 1999 December. According to the test results prepared by Raytheon, the mean read noise measured 15.6 e^- with four Fowler pairs for an 11 s integration, which means that the system can be background-limited, even at high resolution at the short-wavelength end of its operating range. The quantum efficiency measured at 7.74 μm is almost 50%. Based on measurements of similar devices, the quantum efficiency should peak near 60% at $\lambda = 10$–20 μm and be above 30% over the 5–25 μm range. The pixel-to-pixel variations in quantum efficiency are $\pm 3\%$ ($1\ \sigma$). The well size is $\approx$190,000 e^- at 1.0 V bias.

The relatively small well size presents a challenge for lower resolution modes. When operating in low-resolution and camera modes at long wavelengths, the incident photon flux can saturate the detector before we can read the entire array. The number of electrons generated by background sky photons (in units of e^- s^{-1} pixel^{-1}) is given by

$$N_{e^-} = \frac{\mathcal{E}\lambda^2 B_\lambda(T) A\Omega}{hcR}\eta_{\rm opt}\eta_{\rm det}, \tag{2}$$

where $\mathcal{E}$ is the emissivity (instrument+telescope+sky), λ is the wavelength of interest, $B_\lambda(T)$ is the Planck function evaluated at the telescope temperature, A is the telescope area, Ω is the solid angle in the sky seen by a pixel, h is Planck's constant, c is the speed of light, R is the resolving power of the spectrograph, $\eta_{\rm opt}$ is the optical efficiency of the instrument, and $\eta_{\rm det}$ is the quantum efficiency of the detector. Taking the worst case of $\mathcal{E} = 1$ (our blackbody calibrator; see § 5.2), $\lambda = 17$ μm, $T = 275$ K, $A = 71{,}000$ cm^2, $\Omega = 0.33$ arcsec^2, $R = 3600$, $\eta_{\rm opt} = 0.2$, and $\eta_{\rm det} = 0.6$, we find a background count rate of 3.6×10^6 e^- s^{-1} pixel^{-1}. If we can read each pixel before it accumulates 100,000 e^-, a 36 Hz frame rate, then we will safely remain in the detector's linear response regime. The minimum settling times after switching the CRC-744 multiplexer addresses lead to a maximum full-frame rate of around 15 Hz. Therefore, the low-resolution modes require partial array readouts, which increase the frame rate almost inversely to the fraction of rows actually read out.

The CRC-744 chip carrier mounts in a 3M Textool socket, the lid of which has been opened at the center to allow light to hit the detector and relieved near the edges to avoid short circuits on the front-surface contact pads. The socket mounts to a G10 header board, which is attached to the LHe-cooled aluminum wall of the cross-dispersion chamber, with the copper ground plane of the board in contact with the wall. When the detector is powered, the board comes to a temperature of about 5 K. We do not have a temperature sensor on the detector chip, but from the detector time constants there is evidence that it is running at a temperature somewhat below the optimal 6–8 K.

4.2. Electronics

To run our detector, we purchased a version of the IR Observer electronics system from Wallace Instruments. The system includes an analog box with clock driver boards, DC bias boards, and preamp boards; a digital box with timing-pattern control boards, 14-bit analog-to-digital converters, and a data storage and co-adder unit; a rack-mounted control computer running Linux; a rack-mounted power supply; and all the cables required to interface the system with the cryostat. The system came equipped with software suitable for lab testing; we describe some of the modifications required for use at the telescope below and in § 4.3.

The electronics step through and read out the detector pixels continuously. The signal from each pixel is amplified in the analog box and transferred to the digital box, where it is con-

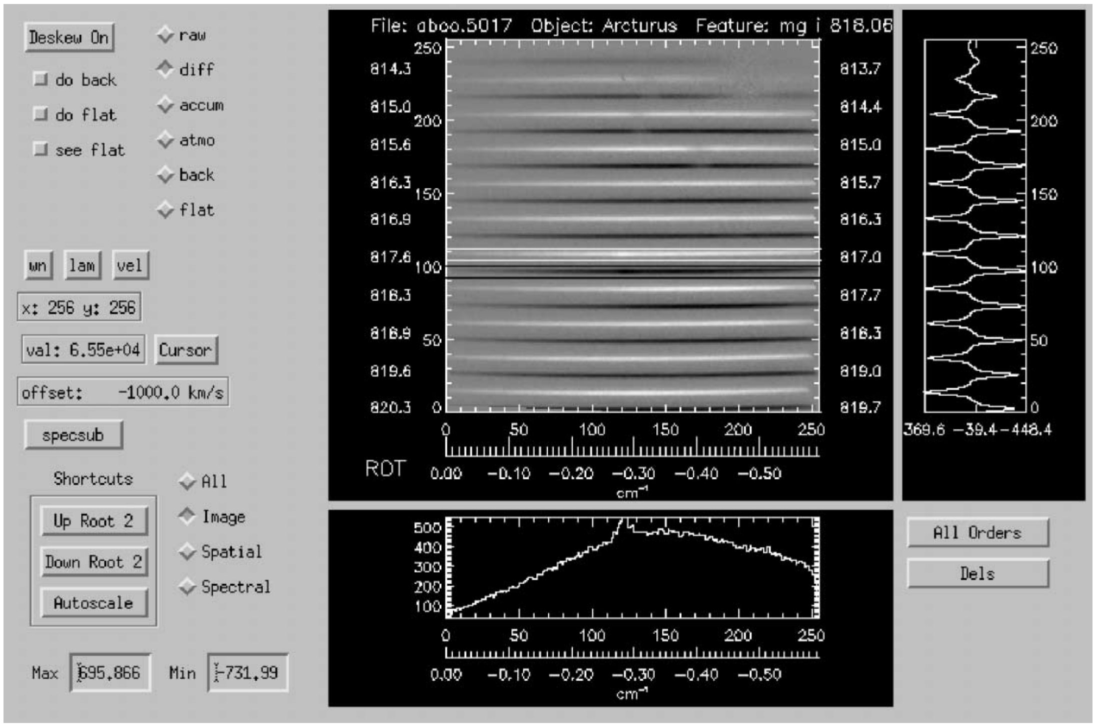

File: aboo.5017 Object: Arcturus Feature: mg i 818.06

x: 256 y: 256

val: 6.55e+04

offset: -1000.0 km/s

Max 695.866 Min -731.99

FIG. 3.—Quick-look GUI with a cross-dispersed spectrum of a star after differencing the two nod beams. The image is rotated in the software to make the dispersion run nearly horizontal. The spectral window below the gray scale displays an extraction of the sixth order from the top. The spatial window to the right shows the wavelength-integrated intensity as a function of position along the slit for each order.

verted to 14-bit digital data and stored as a 32-bit integer in the co-adder buffer. The number of frames combined in the co-adder, "hardware co-adds," is set by the user. Once the appropriate number is reached, the co-adder begins filling a second buffer while the first is asynchronously transferred to the computer. Collecting hardware co-adds currently establishes the minimum unit of time for acquiring data. The continuous detector readout means at least two frames must be discarded each time the telescope is nodded to ensure valid data on every pixel. We added a level of "software co-adds" in the computer to shorten the minimum time unit and improve our observing efficiency. The computer writes the data to disk after the desired number of software co-adds.

Both the array clocking patterns and the patterns for clocking data into the co-adder are controlled by a set of EPROM programs resident in the digital box. Two levels of EPROM programs contain the basic clocking information. The "master" EPROM, a single 8 bit × 256 kbyte chip, contains a series of starting addresses for separate slave routines. The five 8 bit × 256 kbyte "slave" EPROMs operate in parallel and control the clocking levels and the co-adder synchronization and can control a chopping secondary. The hardware can contain 32 8 kbyte master patterns that can select from 32 8 kbyte slave patterns. The patterns currently programmed into the EPROMs include a double sampling (DS) mode, a simple read and reset (single sampling) mode, and partial array readouts. The CRC-744 resets entire rows at a time so that the DS data taking is achieved by reading an entire row, resetting it, and reading it again. In addition, we are testing a Fowler pattern with 16 pairs. If more than 32 patterns are needed, additional EPROM chips must be programmed and swapped into the control board.

4.3. Data Acquisition and Display Software

The data acquisition software for TEXES is divided into two regimes: data taking, involving instrument control and array readout, and data display. Each regime is controlled by a separate computer and is written in a separate software language, determined by the needs of the system. Communications between the two regimes are minimized, allowing for separate development and refinement of each branch of the software. Since TEXES will always be run by someone familiar with the project, our primary goal is for the software to be efficient, with ease of learning being a secondary consideration. We expect to continually improve the software over the life of the instrument.

Data acquisition is governed by the Linux computer mounted on the telescope. This computer controls the detector, operates the instrument, and interacts with the telescope control system. The software provided by Wallace Instruments for running the detector is written in Tcl/tk and C. We chose to write the other control routines in these languages as well. For all control routines, our goal is to allow input from the command line, a graphical user interface (GUI), and scripts.

Motors can be driven locally from a front panel on the electronics rack or remotely by the computer. The “home-grown” control circuit multiplexes three binary input lines to the six motors with addresses for stop and reset. The control circuit passes pulses to individual Vexta motor controllers. When operating remotely, a National Instruments analog and digital I/O board provides the pulses. Registration of the mechanisms is done by counting motor steps and reading, with the same A/D board, 10 V potentiometers linked to the mechanism gear trains. The user is alerted if there is a discrepancy between desired and actual voltage.

The instrument control computer communicates with the telescope to command beam switches and obtain header parameters. At the NASA Infrared Telescope Facility (IRTF), we establish a pipe to use the existing telescope control program.

Once the data have been saved to disk by the instrument control computer, they also are passed to the data reduction program. Our quick-look data reduction is written in IDL running on a Sun workstation and can be operated from the command line or from a GUI (Fig. 3). The GUI has three main display windows: the image of the detector, a collapse of the image along the vertical dimension (the spectral window), and a collapse along the horizontal direction (the spatial window). The quick-look roughly corrects the display so that dispersion runs nearly horizontally and the slit runs nearly vertically. The user can interactively select portions of the detector image to show in more detail in the spectral and spatial windows. It is also possible to display a preliminary spectral extraction of one order. At any time while the data are being collected, the user can switch between displaying a single raw frame, the difference image of a nod pair, or the sum of all nod pair difference images in the current observation.

5. OBSERVATIONS AND DATA REDUCTION

5.1. Observing Modes

TEXES has four basic observing modes: stare, nod, map, and scan, each of which can be used with any of the spectroscopic or imaging instrument modes.

Stare mode involves acquisition of individual frames or co-added sets of frames without any telescope motion. It is used mostly for diagnostic purposes and not for astronomical observations.

In nod mode, the telescope is moved between co-added sets of frames to alternate the object either between two positions along the slit (or within the imaging field) or on and off of the slit. Typically, 4–6 s are spent in each nod position, and 1 s is spent moving the telescope and waiting for it to settle after each motion. Unlike mid-infrared imaging systems for ground-based telescopes, we do not use the chopping secondary. In most weather conditions the systematic fluctuations in the sky emission (sky noise) are less than the photon shot noise at the ∼1/12 Hz nod frequency. Even in nonphotometric weather, sky noise is largely removed by differencing of the two nod beam measurements when one is nodding a source between two points along the slit. We have experimented with multiple-beam nod patterns but do not currently allow this option.

In map mode, the telescope is stepped between nod pairs. The nod throw takes the slit entirely off of the object, and the sky frames preceding and following each source frame are averaged to reduce their contribution to the noise. This mode is used to map extended objects or to search for bright objects.

Scan mode is a variation on map mode but without telescope nodding. The telescope is stepped a long enough distance so that blank sky is observed at one or both ends of the scan, and those observations are used as sky measurements and subtracted from the on-source measurements. In clear weather scan mode can be very efficient. The time spent on sky can be small compared to the total time spent on the source being mapped but large compared to the time spent on each position of the map. Therefore, the noise in the average of the sky frames is small compared to the noise in the source frames from which it is subtracted.

5.2. Calibration

The presence of strong background emission from the sky and telescope limits sensitivity in the mid-infrared. This disadvantage is partially offset by the radiometric calibration that this emission makes possible. We calibrate the measured source emission in a manner very similar to the radiometric scheme used at millimeter and submillimeter wavelengths (e.g., Ulich & Haas 1976). At the beginning of each observing sequence (typically every 10 minutes), a set of calibration frames is taken. These consist of measurements of a black chopper blade, the sky, and a low-emissivity chopper blade just above the Dewar entrance window. The standard procedure is to use the black−sky difference as a flat field. To the approximation that the temperatures $T_{\rm black}$, $T_{\rm telescope}$, and $T_{\rm sky}$ are equal, this flat field serves to correct both for spectral and spatial instrumental gain variations and for the absorption (or blockage) of light by the telescope and the atmosphere, as can be seen from the following:

$$
\begin{aligned}
S_\nu({\rm black} - {\rm sky}) &= \{B_\nu(T_{\rm black}) - [B_\nu(T_{\rm tel})\mathcal{E}{\rm tel} \\
&\qquad + B_\nu(T_{\rm sky})\mathcal{E}(1-\mathcal{E})]\}R_\nu{\rm tel}\nu,\ {\rm sky} \\
&\approx B_\nu(T_{\rm tel})(1-\mathcal{E})(1-\mathcal{E})R_\nu\nu,\ {\rm skytel} \\
&= B_\nu(T_{\rm tel})t_{\rm tel}t_{\nu,\,{\rm sky}}R_\nu . \qquad (3)
\end{aligned}
$$

Consequently, the calibrated source intensity, corrected for the

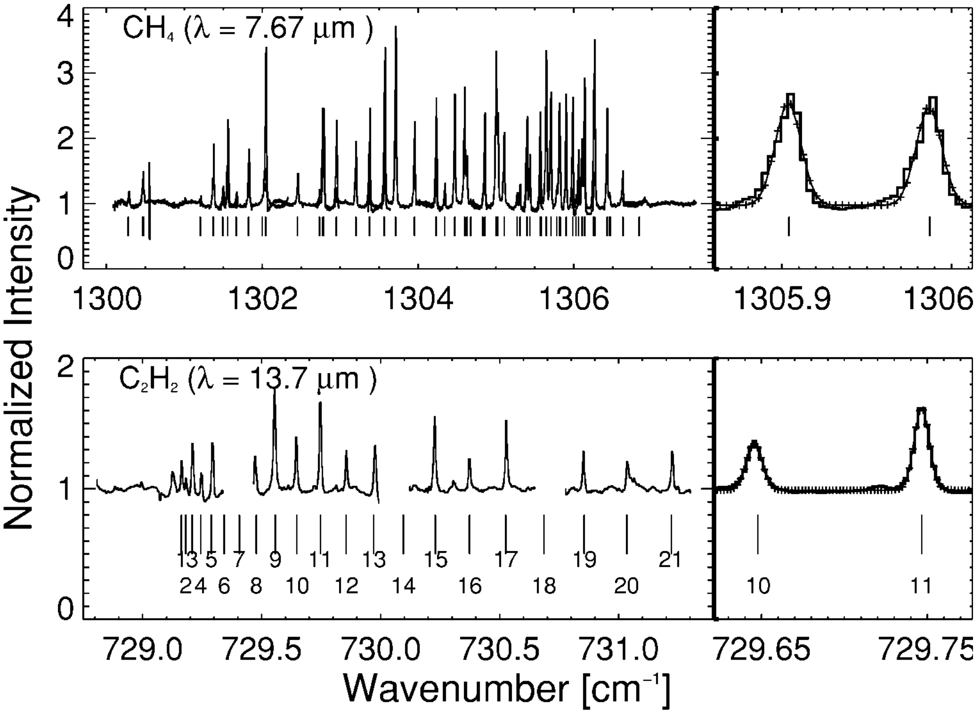

FIG. 4.—Laboratory spectra of the CH_4 *Q*-branch near 7.7 μm (*top*) and the C_2H_2 *Q*-branch near 13.7 μm (*bottom*). The left panels show roughly 60% of the coverage, and the right panels show Gaussian fits to selected lines for each molecule. The short-wavelength line profiles are non-Gaussian, particularly on the red edge. For CH_4 the FWHM of the best-fit Gaussian gives $R = 75{,}000$, while for C_2H_2 the FWHM gives $R = 100{,}000$.

transmission of the telescope and sky, is given by

$$I_\nu(\mathrm{obj}) \approx S_\nu(\mathrm{obj} - \mathrm{sky}) \frac{B_\nu(T_{\mathrm{tel}})}{S_\nu(\mathrm{black} - \mathrm{sky})}, \qquad (4)$$

where S_ν is the measured signal, $B_\nu(T)$ is the blackbody function at temperature T, $\mathcal{E}$ is the emissivity of the telescope or sky, R_ν is the instrumental responsivity, and $t = 1 - \mathcal{E}$ is the transmission of the telescope or sky.

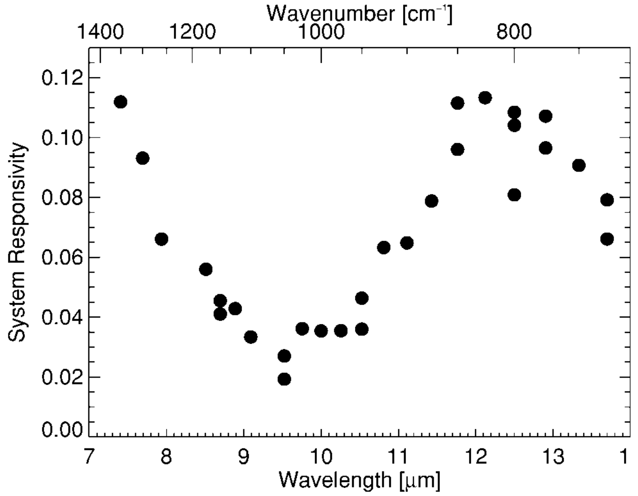

FIG. 5.—TEXES's system response in the 8–13 μm range as determined from a blackbody. This response is near the peak of the echelon blaze. For wavelengths far off blaze, the response can be a factor of 2 lower.

The flat-fielding procedure reduces the depths of H_2O lines by ~80%, CO_2 and N_2O lines by ~50%, and O_3 lines by ~20% (since these molecules are low, mixed, and high in the atmosphere, respectively, and thus are at different temperatures). It should be possible to remove the residual atmospheric absorption by dividing by comparison stars. Unfortunately, we have found that nearly all stars bright enough to serve as good comparisons (mostly K and M giants and supergiants) have photospheric or circumstellar H_2O, with lines throughout the mid-infrared. Instead, we have begun to use asteroids as atmospheric comparison sources. They appear to work well for this purpose, especially at our longer wavelengths, where they are bright.

5.3. Pipeline Data Reduction

The data stored during observations are from the Wallace Instruments co-adder, with both sides of each nod pair appended to a disk file during an observing sequence. A pseudo-FITS header is stored separately from each binary data file.

First-pass data reduction is carried out by a pipeline reduction program written in Fortran. The pipeline reduction involves the following steps:

1. Read in the calibration (flat-field) frames and their header.
2. Use the *black* frame to locate echelon orders and check

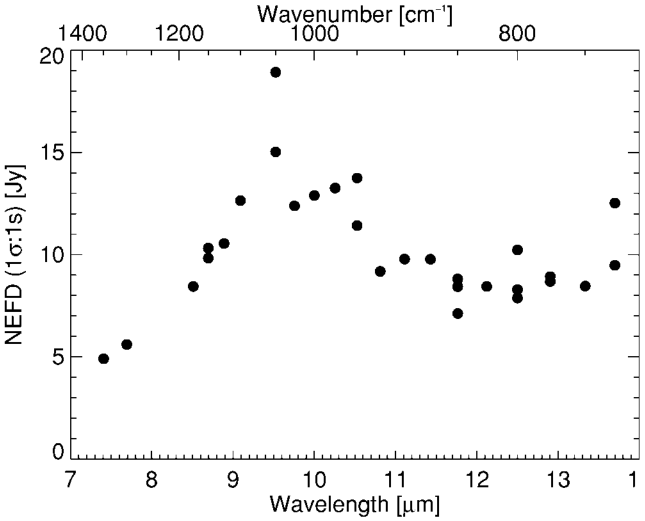

FIG. 6.—Calculated NEFD based on blackbody measurements and assumptions as given in the text.

distortion parameters, particularly the order rotation caused by the K mirror.

3. Derive a calibration image from black−sky.
4. Read in the object header and data frames.
5. Search for and correct spikes in individual frames.
6. Optionally attempt to correct for optics bounce.[1]
7. Difference the two beam measurements of each nod pair.
8. Interpolate over dead or noisy pixels.
9. Calibrate and flat-field the data frames with the calibration frame.
10. Correct for optical distortions (this is based on data stored in the headers and knowledge of the optical design of the instrument and is accurate to better than 1 pixel over most of the array).
11. Optionally shift each nod difference frame in the spatial direction to correct for guiding errors along the slit.
12. Add nod pairs together, optionally weighted by the continuum signal in each nod pair.
13. Extract a spectrum from the difference frame, optionally weighted by the distribution of the continuum signal along the slit.
14. Optionally ask the user to mark the position of an atmospheric line in the calibration frame to set the wavenumber scale.
15. Store the difference frame and extracted spectrum.
16. Optionally add the difference frame and extracted spectrum to a running average for an object.

An important feature of the pipeline reduction is that it requires very little user intervention while accurately correcting for optical distortions, deriving a linearized spectrum, and optimally weighting nod pairs and the distribution of the signal along the slit to maximize the final signal-to-noise ratio. Normally, the user simply makes up a script file with flags for options and names of files to be reduced, then runs the program. User intervention is required only to specify an atmospheric line for accurate wavenumber calibration. The pipeline reduction requires about 1 hr of Sun Ultra 5 CPU time to reduce a night's data. Data can be reduced during or immediately after a night of observations, so instrument users will leave the telescope with understandable spectra. Further custom reduction, e.g., selection and combination of observation sets, customized extraction of spectra, and division by comparison objects, is done with whatever software the user chooses.

6. PERFORMANCE

After our first experience at the telescope, we found that astronomical objects generally are poor tests for TEXES's spectral resolution. Therefore, we made a gas cell that mounts over the Dewar entrance lens to test the spectral resolution, internal instrument focus, and mechanism zero points. The cell consists of a Teflon cylinder of ∼2 inch diameter and 1 inch length, which is sealed to the window with an O-ring and which is terminated with a mirror that looks back into the cold Dewar. The cell can be evacuated and then filled with low-pressure gas. The mirror arrangement provides a low background, allowing very weak molecular thermal emission lines to be seen much more easily than in an absorption cell. Example emission-line spectra of CH_4 (7.67 μm) and C_2H_2 (13.7 μm) are shown in Figure 4. Gaussian fits to the data give an FWHM of 0.007 cm^{-1} at 13.7 μm ($R = 100{,}000$). Shortward of 8 μm, the best-fit Gaussian has a width corresponding to $R = 75{,}000$, but the line profile systematically has extra power in a red wing. This behavior is expected given the groove-spacing errors in the echelon.

The response of the instrument, both to blackbody radiation and to starlight, is consistent with an overall efficiency of the optics and detector of ∼10% at wavelengths near 8 μm and longward of 12 μm. However, the efficiency drops by a factor of up to 4 in a broad trough between these wavelengths (Fig. 5), an effect we do not yet understand but are investigating. In high-resolution, cross-dispersed mode, the measured noise is consistent with the calculated photon shot noise, given the measured efficiency. However, much higher noise is observed in medium- and low-resolution modes. The output of the detector array becomes very spiky above a photocurrent threshold near the level observed in medium-resolution mode, increasing the noise by more than 1 order of magnitude. Reducing the effective bias across the array improves the behavior but compromises the response in high-resolution mode. Until

---

[1] In cross-dispersed mode, very small shifts in the optics between nod beams can cause spurious signals from imperfect background cancellation in the regions of steep variation of the background at the edges of echelon orders (see § 6). We have had some success in removing this effect by shifting or smoothing the measured data in one nod beam relative to the other before differencing. However, a nodded source can be interpreted by the software as optics bounce, especially if it comes near the ends of the slit, so bounce correction must be used with caution.

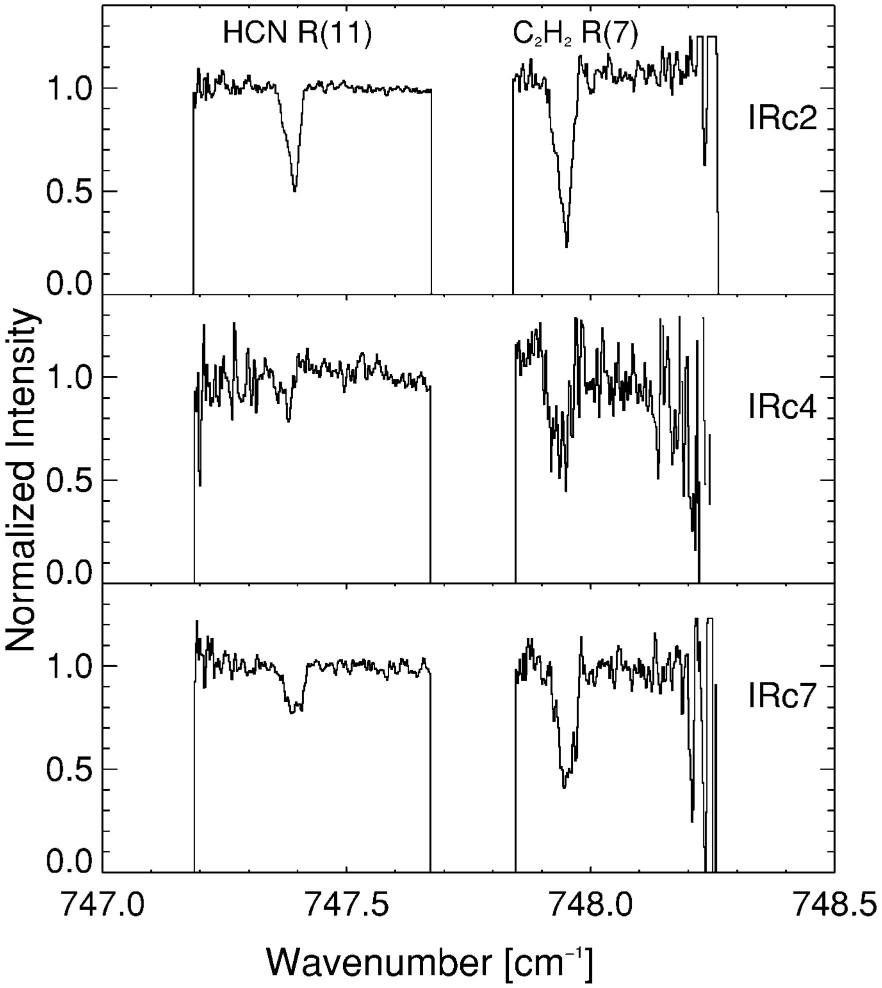

FIG. 7.—High-resolution spectra showing C_2H_2 and HCN absorption along the line of sight to Orion IRc2, IRc4, and IRc7. Two orders of six are displayed in each case. Atmospheric emission and absorption cause the rise in noise near the ends of the region plotted, but the structure near the C_2H_2 line is real.

we find a better solution, we plan to adjust the bias depending on the observing mode.

Figure 6 shows the noise equivalent flux density (NEFD) for our high-resolution mode. These data are derived from signal-to-noise ratio measurements during observation of a blackbody and calculation of the NEFD taking parameters appropriate to TEXES on the IRTF: system emissivity of 0.10, atmospheric transmission of 100% (true in much of the window), slit losses of 20%, resolving power of 100,000, and a 3 m telescope. The NEFD is appropriate for on-source time during nodding of the telescope. A nodding efficiency parameter (30%–80% depending on conditions and target extent) must be included when one estimates clock time. The NEFD will scale roughly as the square root of the total emissivity (including the increased emissivity from the atmosphere on terrestrial lines) and inversely with the telescope diameter squared. Therefore, TEXES observing on an 8–10 m telescope with 5% emissivity (our foreoptics contribute 5% emissivity) should give an order-of-magnitude improvement in the NEFD or a factor of 100 in time.

We have conducted numerous tests on the repeatability of mechanisms and the dependence of flexure of elements with time and telescope position. The slit wheel motions are reproducible to the 1 pixel level. Filter positioning is satisfactory with respect to the choice of slit length, but positioning of the CVF to maximize throughput still must be done by finding half-power points. This may simply be the result of an incorrect dispersion relation in the CVF positioning software, but further tests need to be done. The echelle and first-order grating come to the desired position within a few pixels. We typically confirm grating positioning using sky frames that show telluric emission lines. The K-mirror assembly is the most prone to positioning errors, primarily because of backlash in the gear train. Although we have generally tried to remove backlash by forcing the motor control software to always travel the same direction before stopping, something more must be done for this mechanism.

In general, flexure within the instrument and between the instrument and the telescope guide camera is acceptable. By

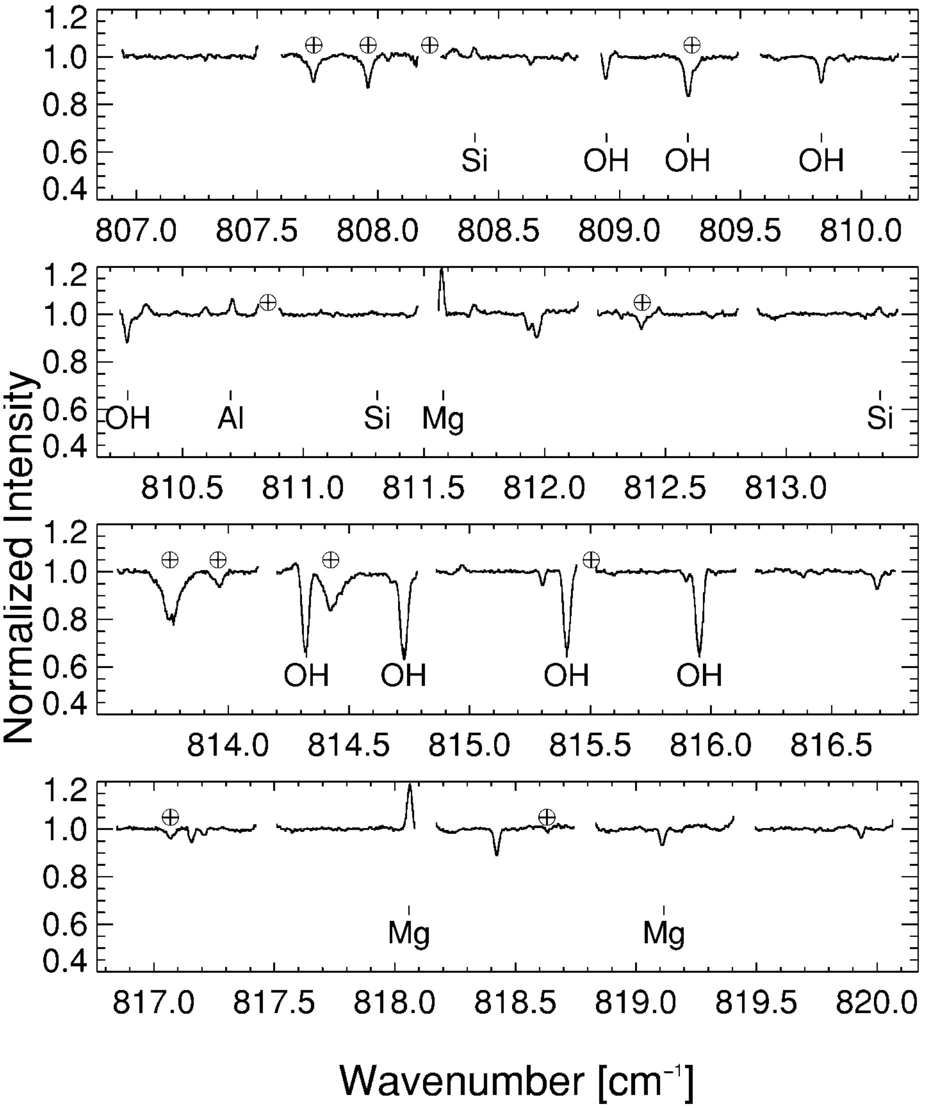

FIG. 8.—High-resolution spectrum of Arcturus using the first-order grating as the cross-disperser. Telluric lines (*circled plus signs*) are indicated. Some stellar features are labeled, with most of the unlabeled absorption lines being due to water.

imaging a pinhole and slewing $\pm 1^{\mathrm{h}}\!.5$ east-west from zenith, we determined that the internal flexure between our slit and the focal plane is ≈1 pixel for the full 45° motion. After peaking on the infrared radiation of a bright star and setting the telescope camera crosshairs on the visible signal, we found that a 60° motion (east-west) resulted in a $1''$ error in positioning while a 40° motion (north-south) resulted in a $2''$ error. During this test, the seeing was fairly poor, $\approx 1\overset{\prime\prime}{.}3$, so while the results are not definitive, they are certainly tolerable.

The major problem with flexure, or possibly other internal motion, comes with the echelle grating or its associated paraboloid. When one observes the same source for 1 hr, a 1 pixel shift is apparent along the echelle dispersion direction. Because our flat-fielding and atmospheric corrections are done with calibration images taken at the start of each observation (§ 5.2), this drift effectively limits observations to ~15 minutes before additional calibration images are required. We see no such drift in the direction of the echelon dispersion, suggesting that the echelle grating is moving.

A more serious problem can arise when the echelle grating appears to bounce in response to telescope nodding. Because the contrast between illuminated and unilluminated regions of the focal plane is so large, any shifts in the illumination pattern between the two nod beams result in large systematic features in the difference image. We have seen two types of bounce: one consistent with a systematic shift in the echelle's position between the two nod beams and the other consistent with a shaking of the echelle throughout one of the two nod beams. These problems seem to be more common when one observes near the meridian at substantial air mass and nods along a north-

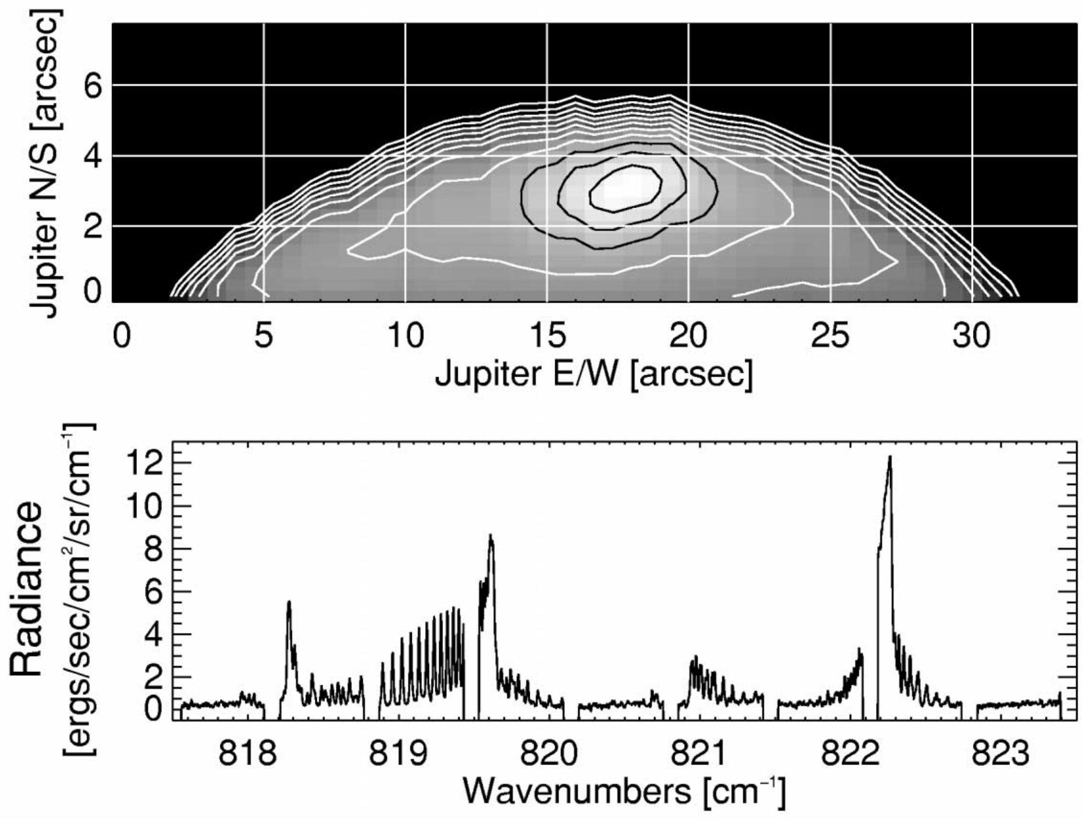

Fig. 9.—*Top:* Scan across the northern limb of Jupiter. The slit was oriented along the planetocentric north/south direction and was stepped $\frac{2}{3}''$ from east to west. The bright region is an enhancement due to the North Auroral Ring. *Bottom:* Ethane spectrum corresponding to a pixel in the middle of the bright enhancement above.

south slit. We have not had the engineering time required to test the conditions for causing the bounce but have developed a software fix (see § 5.3).

6.1. Selected Astronomical Observations

To date, TEXES has had 8 nights on the McDonald Observatory 2.7 m telescope and 35 nights on the NASA IRTF for a mix of engineering and science. We present here observational results from some of the projects in progress.

In Figure 7, we present data from the project for which the instrument was designed: molecular absorption along the line of sight to embedded star-forming regions. Two orders of the six observed toward the KL region of Orion are presented, one with the C_2H_2 $R(7)$ line and one with the HCN $R(11)$ line. Both lines are clearly resolved and show non-Gaussian line profiles composed of several very narrow components. These facts contradict assumptions in the analysis of Irshell data (Evans, Lacy, & Carr 1991; Carr et al. 1995). These data came from less than 20 minutes of integration time. We have substantially more time in 2001 November at the IRTF to examine the absorption behavior toward Orion in more detail. Other targets will be presented in a paper by N. J. Evans et al. (2002, in preparation).

As mentioned above, most late-type stars are full of spectral features in the mid-infrared; Figure 8 illustrates this point with a “hi-lo” (high-resolution grating cross-dispersed by the first-order, low-resolution grating) spectrum of Arcturus. Arcturus is a K1.5 III star and so is moderately hot by the standards of mid-infrared spectroscopy. We show 20 of the 22 orders recorded in a single grating setting with terrestrial lines marked and many stellar lines labeled. The strongest emission lines are from Mg I, and the strongest absorption lines are OH. Most of the unlabeled absorption lines come from H_2O. This observation contains 180 s on-source integration time. The emission lines may be important to magnetic field measurements (Carlsson, Rutten, & Shchukina 1992; J. A. Valenti et al. 2002, in preparation). J. H. Lacy et al. (2002, in preparation) will examine H_2O abundances and kinematics for late-type stars.

TEXES will be a very effective instrument for studying the atmospheres of planets. In Figure 9 we show a map of Jupiter’s northern limb summed over the spectral region 818.0–820.0 cm^{-1} (12.195–12.225 μm), which includes continuum and ethane line emission. By using the scan mode, we are able to observe a slice across the disk of Jupiter and look for latitudinal and longitudinal variations. By observing

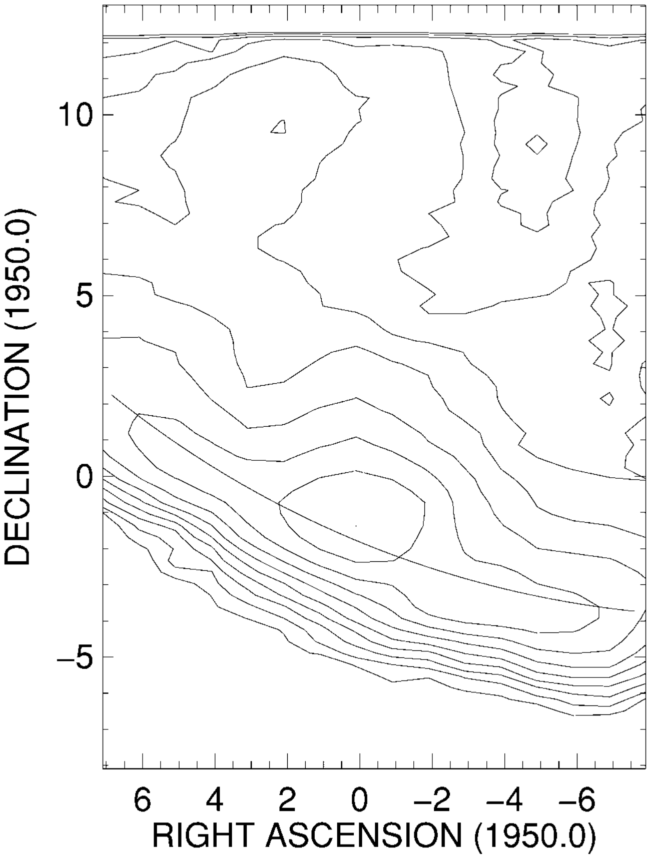

FIG. 10.—[Ne II] (12.8 μm) line map of Mon R2 IRS 1 integrated over all velocities. Contours are drawn at 0.5, 0.35, 0.25, 0.17, 0.125, 0.088, 0.0625, and 0.044 of the peak value. Pixel values along the curve are used for the position-velocity diagram in Fig. 11.

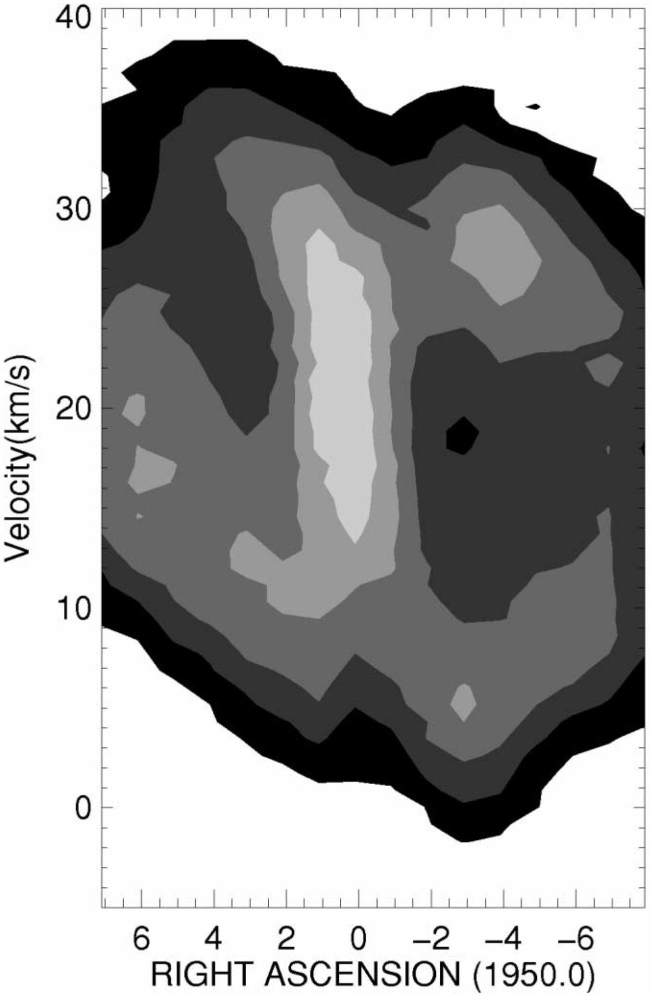

FIG. 11.—Position-velocity diagram through the strong arc of emission in Mon R2 IRS 1. The contours are drawn at intervals of $\frac{1}{6}$ of the peak value.

multiple lines of various molecules at high spatial and spectral resolution, we can investigate the atmospheres in more detail than was previously possible (T. K. Greathouse et al. 2002, in preparation).

Another class of objects that will benefit from high spectral and spatial resolution study in the mid-infrared is that of ultracompact H II regions. These objects contain a massive star deeply embedded in gas and dust and creating a very compact, high-density region of ionized gas. Given the extinction, most of our knowledge of these regions comes from radio continuum and recombination line observations, as well as infrared imaging. We observed one such region, Mon R2 IRS 1, in the [Ne II] fine-structure line at 780.4 cm^{-1} (12.814 μm). The observations were done using the map mode in roughly 8 minutes of clock time. The velocity-integrated map (Fig. 10) shows structure very similar to what is seen in the radio continuum and near-infrared recombination lines (Massi, Felli, & Simon 1985; Howard, Pipher, & Forrest 1994). However, the position-velocity diagram (Fig. 11) demonstrates that [Ne II] observations give considerable additional information. In this case, we see that the line is broad and centrally peaked where the emission is strongest, but becomes double peaked with comparatively little emission at the central velocity away from the peak. Interpretation of these data will be in Q. Zhu et al. (2002, in preparation).

The fabrication of TEXES was supported primarily by the National Science Foundation, with additional support from the National Aeronautics and Space Administration through the Universities Space Research Association. Observations with TEXES were supported by the Texas Advanced Research Program. We thank Bianca Basso, Wanglong Yu, Jimmy Welborn, George Barczak, and Doug Edmonston for their able assistance.

REFERENCES

Bach, K. G., Bach, B. W., & Bach, B. W. 2000, Proc. SPIE, 4014, 118

Becklin, E. E. 1997, in The Far Infrared and Submillimetre Universe, ed. G. Prilbratt, S. Volonte, & A. Wilson (ESA SP-401; Noordwijk: ESA), 201

Born, M., & Wolf, E. 1980, Principles of Optics (Oxford: Pergamon)

Carlsson, M., Rutten, R. J., & Shchukina, N. G. 1992, A&A, 253, 567

Carr, J. S., Evans, N. J., II., Lacy, J. H., & Zhou, S. 1995, ApJ, 450, 667

Evans, N. J., II, Lacy, J. H., & Carr, J. S. 1991, ApJ, 264, 485

Gassner, R. H., & ASM Committee on Heat Treating of Aluminum Alloys. 1964, in Metals Handbook Volume 2: Heat Treating, Cleaning and Finishing, ed. T. Lyman (8th ed.; Metals Park: Am. Soc. Metals), 271

Howard, E. M., Pipher, J. L., & Forrest, W. J. 1994, ApJ, 425, 707

Lacy, J. H., Achtermann, J. M., Bruce, D. E., Lester, D. F., Arens, J. A., Peck, M. C., & Gaalema, S. D. 1989, PASP, 101, 1166

Lacy, J. H., Richter, M. J., Yu, W., & Basso, B. S. 1998, Proc. SPIE, 3354, 436

Lahuis, F. & van Dishoeck, E. F. 2000, A&A, 355, 699

Massi, M., Felli, M., & Simon, M. 1985, A&A, 152, 387

Michelson, A. A. 1898, ApJ, 8, 37

Mumma, M. J., Kostiuk, T., Buhl, D., Chin, G., & Zipoy, D. 1982, Opt. Eng., 21, 313

Ridgway, S. T., & Brault, J. W. 1984, ARA&A, 22, 291

Ulich, B. L., & Haas, R. W. 1976, ApJS, 30, 247

Wu, J., Forrest, W. J., Pipher, J. L., Lum, N., & Hoffman, A. 1997, Rev. Sci. Instrum., 68, 3566